Supplementary Information (SI) for Journal of Materials Chemistry A.

SUPPORTING INFORMATION

Spatial Decoupling-Engineered MOF-Based Nanofibrous Membranes: In-Situ Construction of a Self-Alkaline Microenvironment for Real-Time Nerve Agent Simulant DMMP Degradation

Yunxiao Zhu,[a,1] Panpan Li,[a,1] Cunyi Zhao,[a,b] Jianyong Yu,[a,b] Yang Si,[a,b]

[a] State Key Laboratory for Modification of Chemical Fibers and Polymer Materials, College of Textiles, Donghua University, Shanghai 201620, China

[b] Innovation Center for Textile Science and Technology, Donghua University, Shanghai 200051, China

Corresponding authors:

E-mail addresses: yangsi@dhu.edu.cn (Y. Si), yujy@dhu.edu.cn (J. Yu).

[1]These authors contributed to this work equally.

Supplementary information contains:

Supplementary Figures: S1-S17

Supplementary Video: S1-S2

Supplementary Table: S1-8

Supplementary Note: 1-5

Supplementary Figures:

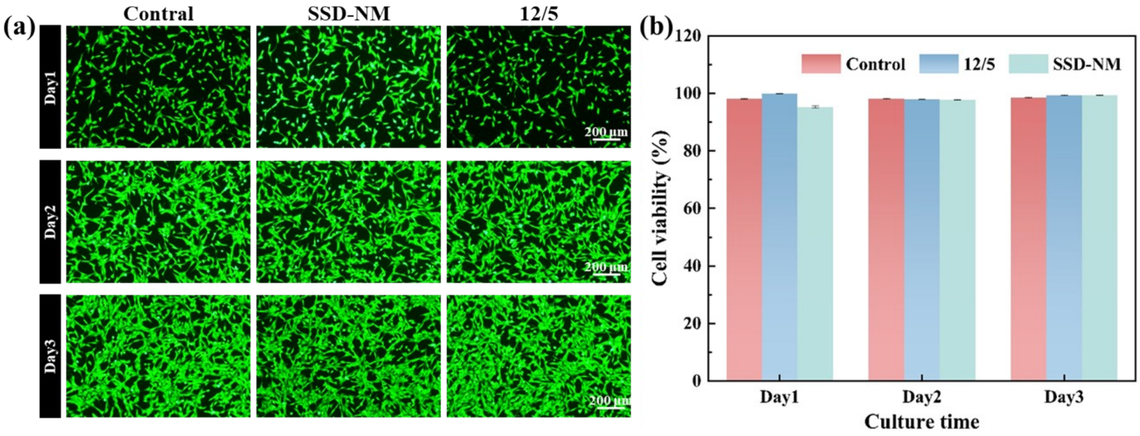

Figure S1. In vitro cytotoxicity assessment. (a) Fluorescence microscopy images of cells cultured with Control, SSD-NM, and 12/5 extracts for 1-3 days (scale bar: 200 μm). (b) Cell viability measured by CCK-8 assay for Control, 12/5, and SSD-NM over 3 days. Data are mean ± SD (n = 3).

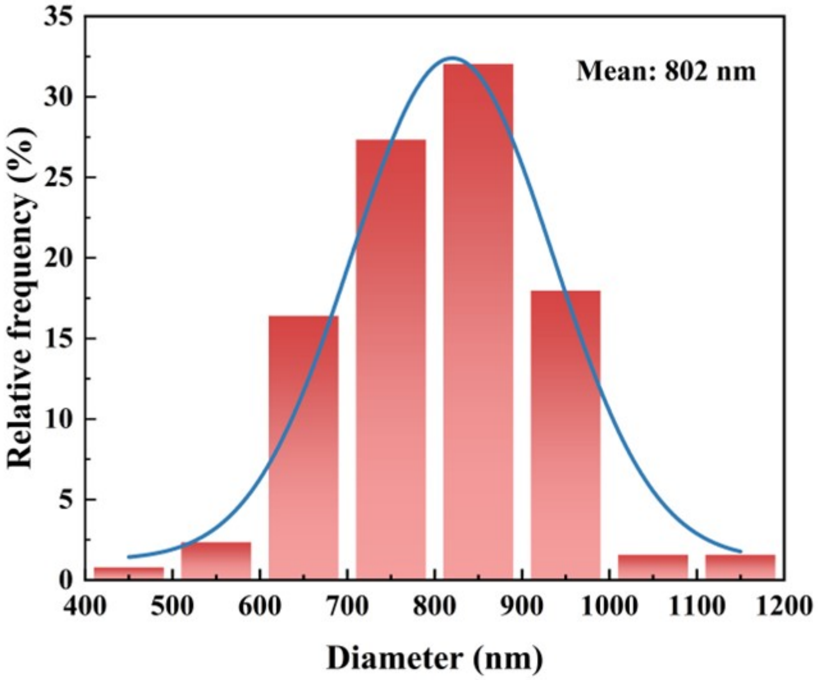

Figure S2. Particle size distribution histogram of MOF-808 nanocrystals.

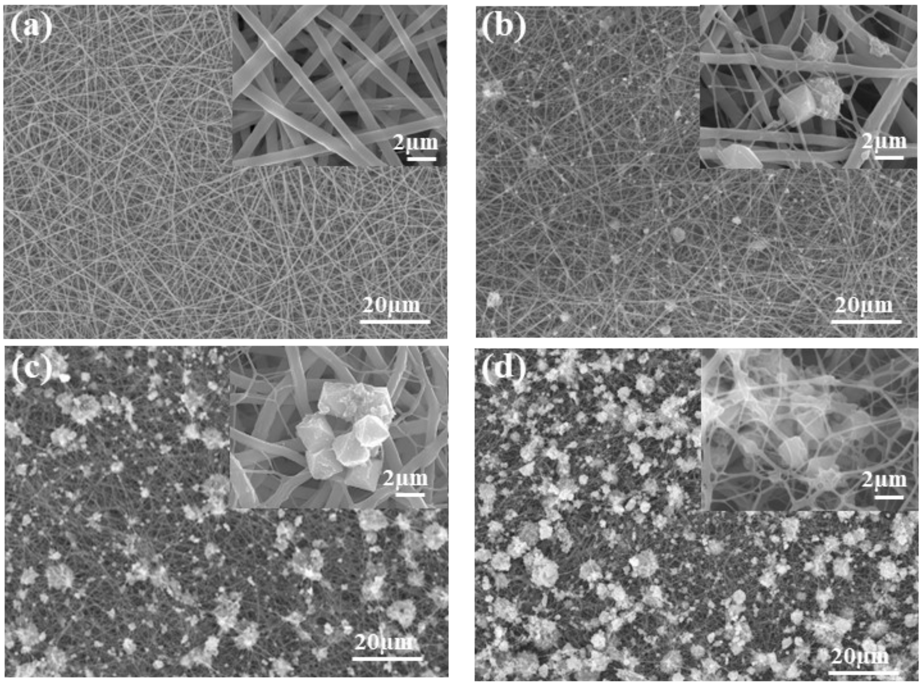

Figure S3. SEM images of nanofibrous membranes with different MOF-808 loadings: (a) 12/0, (b) 12/3, (c) 12/5, and (d) 12/7.

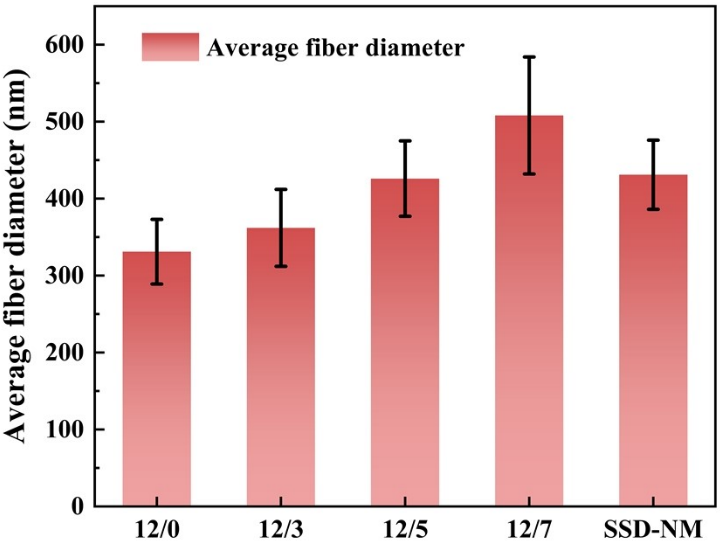

Figure S4. Average fiber diameter of TPU/MOF nanofibrous membranes with different MOF-808 loadings (12/0, 12/3, 12/5, 12/7) and SSD-NM.

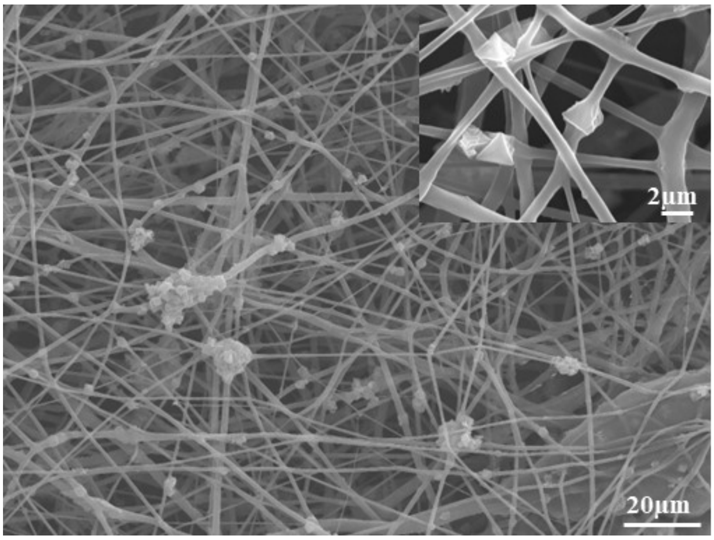

Figure S5. SEM images of TPU/MOF-12/5 composite nanofiber membrane.

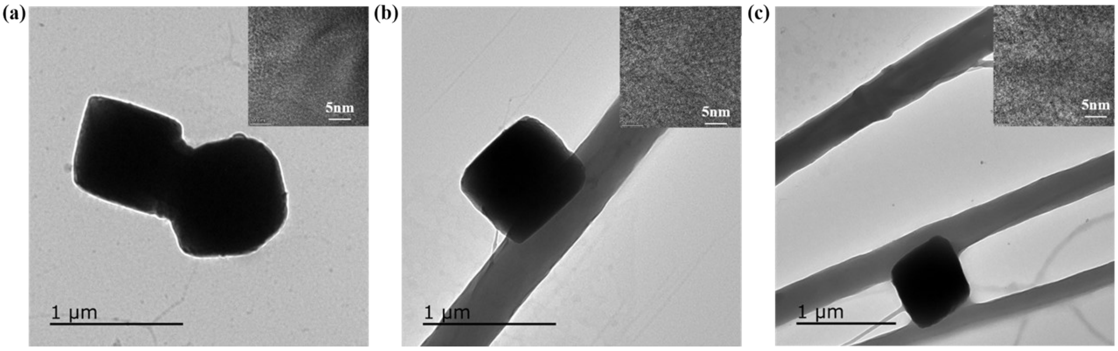

Figure S6. TEM images of (a) MOF-808 nanocrystals, (b)12/5 and (c) SSD-NM.

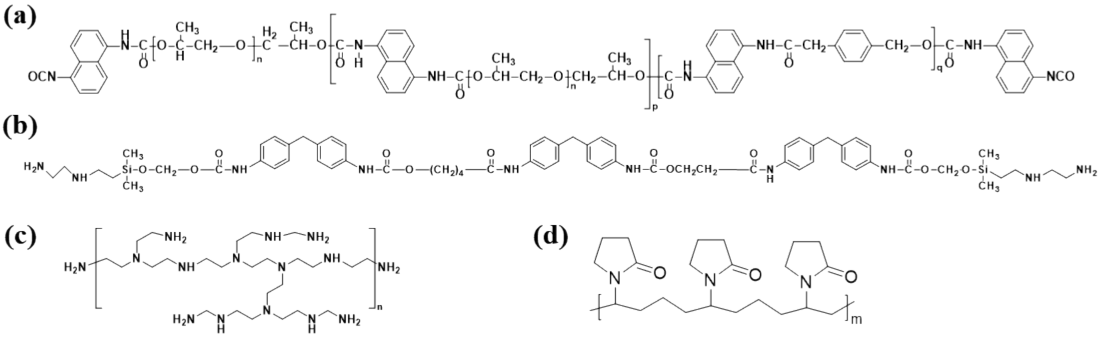

Figure S7. The molecular structures of the SSD-NM material. (a) TPU. (b) hydrophobing agent. (c) PEI. (d) PVP.

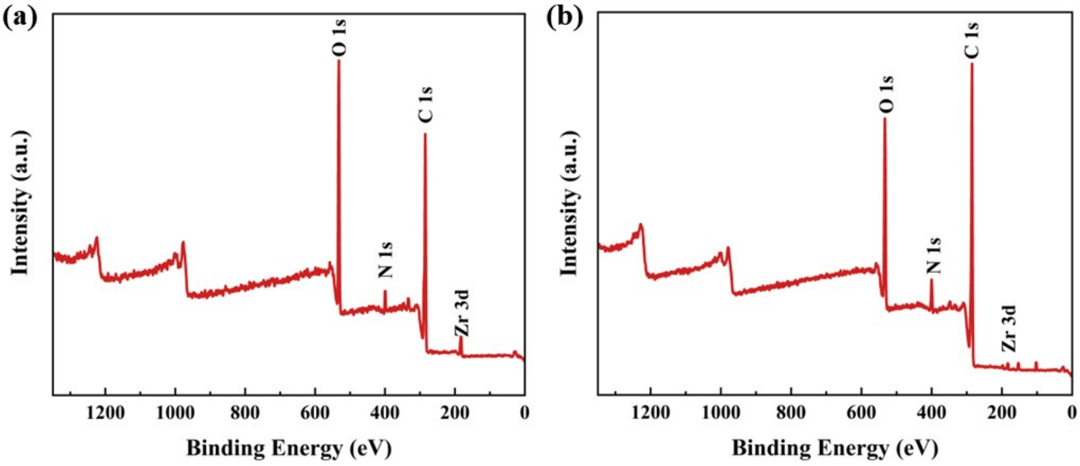

Figure S8. XPS spectra of (a) 12/5 nanofibrous membranes and (b) SSD-NM for all elements.

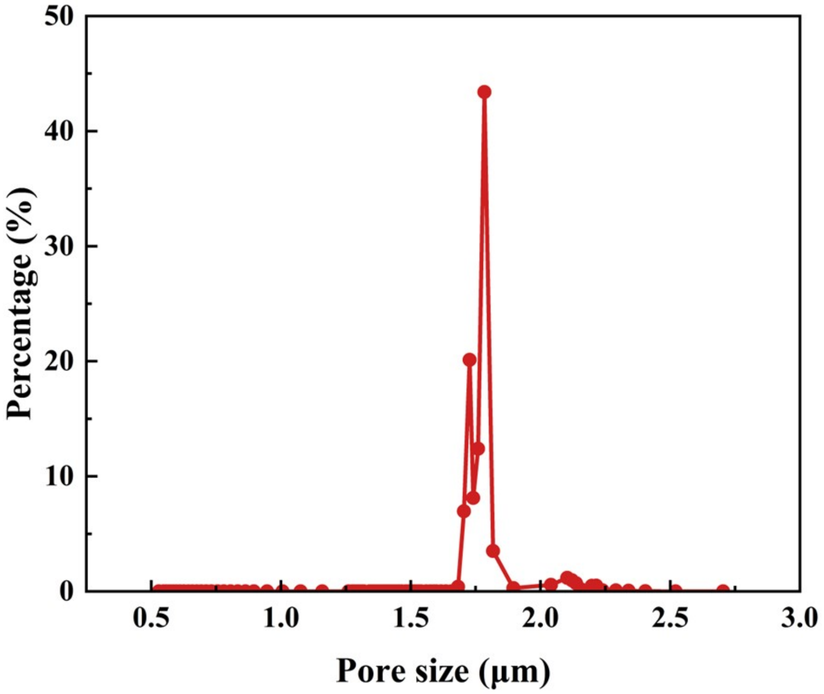

Figure S9. Pore size distribution curves of TPU/MOF-12/5 composite nanofiber membrane.

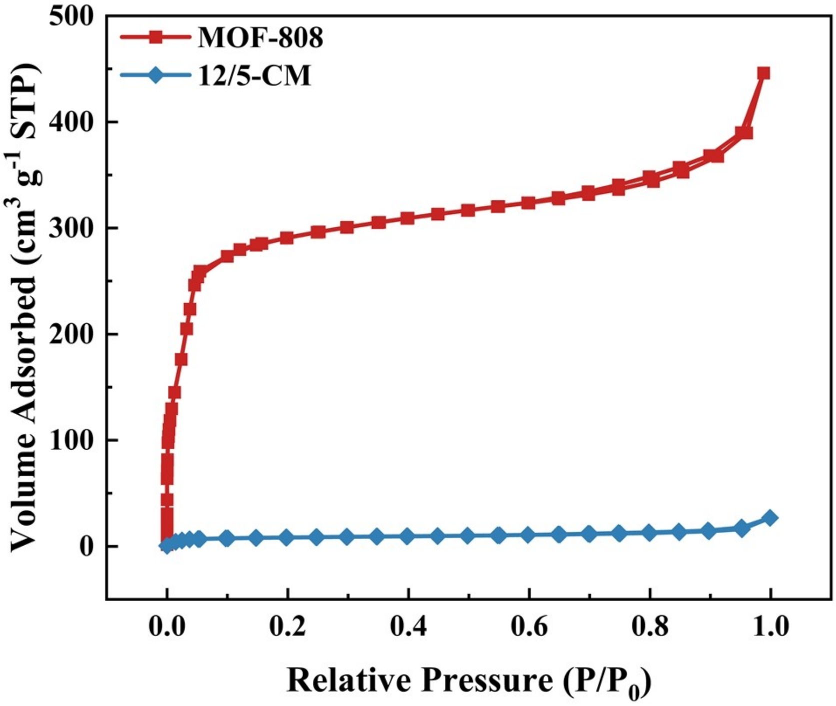

Figure S10. Nitrogen adsorption-desorption isotherms of MOF-808 particles and 12/5 composite membranes (12/5-CM).

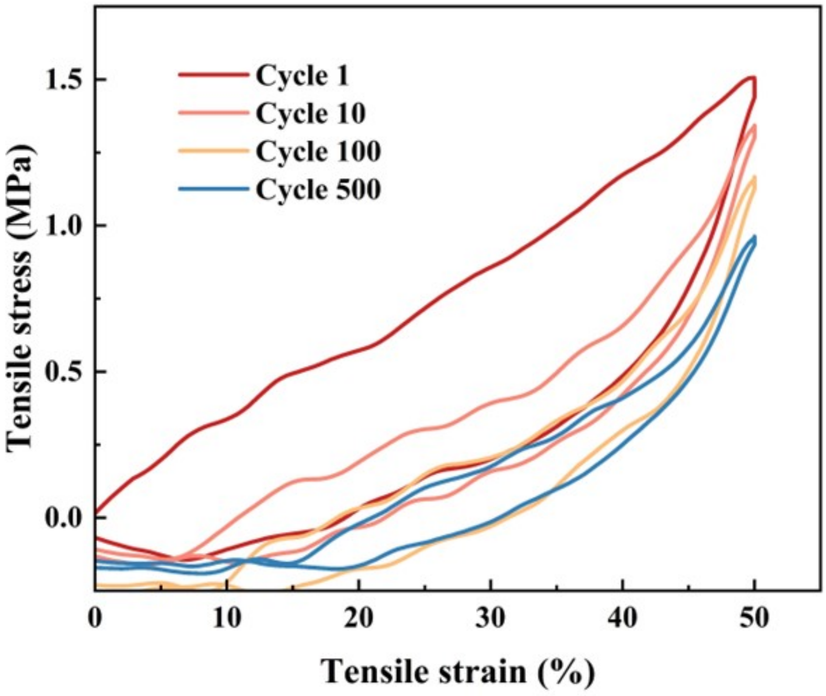

Figure S11. Performance of the SSD-NM after 500 loading-unloading tensile cycles.

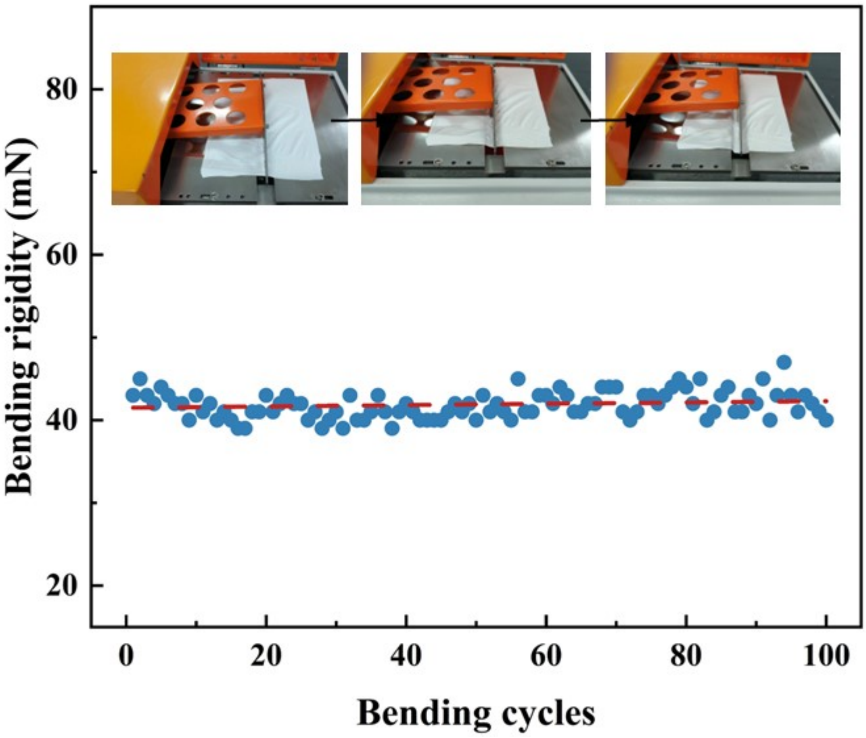

Figure S12. Bending rigidity of SSD-NM as a function of bending cycles, showing stable flexibility over 100 cycles.

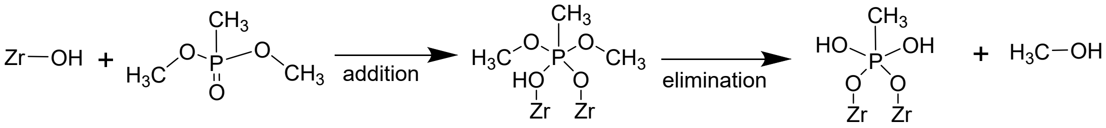

Figure S13. The sketch of the essential steps in the reaction mechanism for degradation of DMMP on MOF-808

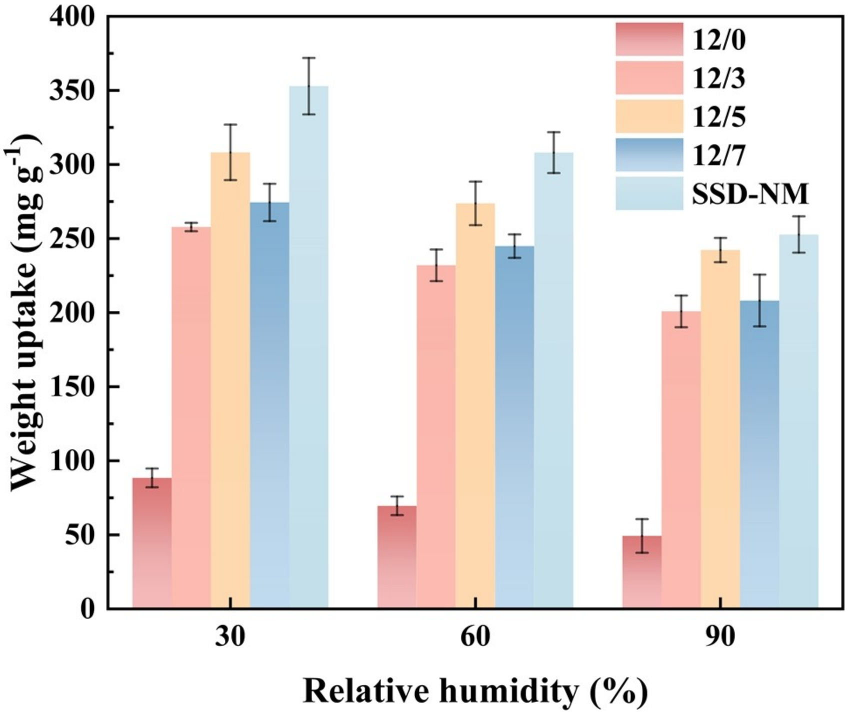

Figure S14. DMMP adsorption capacity of TPU/MOF membranes under varying relative humidity (30%, 60%, and 90%). Data are presented as mean ± standard deviation (n = 3).

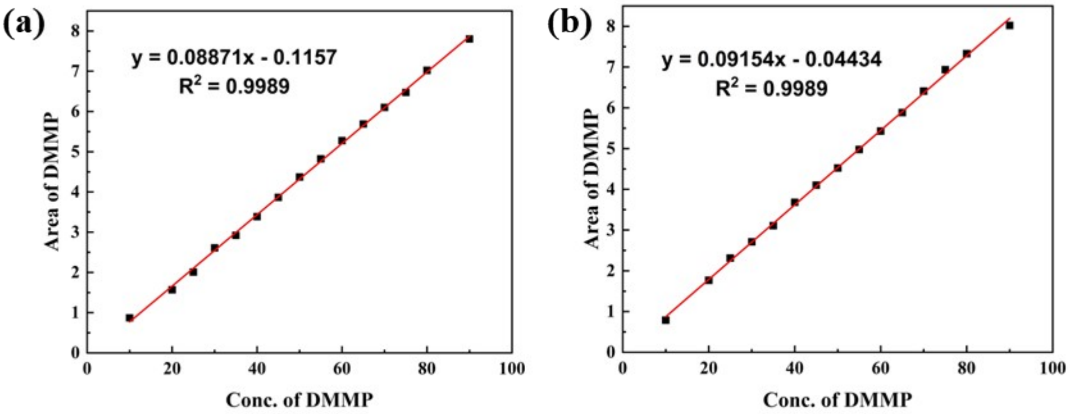

Figure S15. GC-MS calibration curves for DMMP. (a) Standard solution without N-ethylmorpholine (NEM). (b) NEM-containing solution; linear fit after outlier exclusion. R² = 0.9989

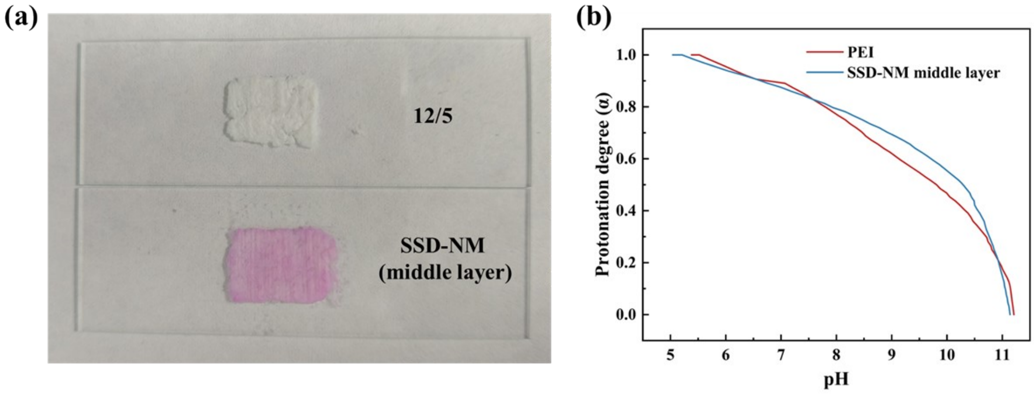

Figure S16. (a) Phenolphthalein coloration of 12/5 and the SSD-NM middle layer. (b) Protonation degree (α) versus pH profiles for PEI and the SSD-NM middle layer.

Figure S17. Large-scale sample picture of the SSD-NM.

Supplementary Videos:

防水透湿视频.mp4

Video S1. Demonstration of the waterproofing effect of SSD-NM.

拉伸.mp4

Video S2. Tensile deformation and fracture behavior of SSD-NM during uniaxial stretching.

Supplementary Table:

Table S1. Microstructural parameters of nanofibrous membranes with different mof-808 loadings and fabrication method.

Sample	Average pore size /μm	Maximum pore size /μm	Porosity /%	Brunauer-Emmett-Teller (BET) / $m^2 \cdot g^{-1}$
TPU/MOF-12/0	1.24	1.74	62.8	3.02
TPU/MOF-12/3	0.97	1.41	74.7	63.27
TPU/MOF-12/5	0.94	1.41	95.8	223.01
TPU/MOF-12/7	0.96	3.47	74.0	151.10
SSD-NM	0.80	1.21	90	204.66
TPU/MOF-12/5 composite nanofiber membrane	1.78	2.70	43.4	32.58

Table S2. Comparison of Half-Life Data for Various Materials: Sources and Test Conditions.

Material	Half-life (min)	Simulant	Test Conditions	Reference
Im-72@DHP-UiO	1.8	DMNP	Buffer-free	J. Dai et al.[1]
SSD-NM	**6.18**	**DMMP**	**Buffer-free**	**This work**
PMMA-BPEI/UiO-66	8.4 (liquid phase); 288 (humid environment)	MPO	Liquid phase / 99% RH humid environment	J. Y. Seo et al.[2]
Im@DHP/Fiber	19.6	DMNP	Ambient humidity (solid/fiber state)	J. Dai et al.[1]

JLMF	33.6 (0.56 h)	DMNP	90% RH, atmospheric environment	X. Wang et al.[3]
MOF-808/PEI/fiber	96 (1.6 h)	DMNP	Humid conditions (50% RH)	Z. Chen et al.[4]

Table S3. Comparison of Hydrostatic pressure Data for Various Materials: Sources

Material	Hydrostatic pressure (kPa)	Reference
AN/IPDI/ASO	64.4	H. Liao et al.[5]
SSD-NM	**89.22**	**This work**
Si-PU/PMMA/PVB)	65.29	G. Ren et al.[6]
Si-PU	52	D. Lu et al.[7]
BPU	48.2	B. Zhang et al.[8]
AMP/MDI	93.8	L. Zhang et al.[9]

Table S4. Spatial distribution of key properties across a 50 × 40 cm large-area SSD-NM membrane.

Region	Thickness (μm)	Hydrostatic pressure (kPa)	DMMP degradation (%, 10 min)
1 (upper-left)	139.16 ± 7.66	87.35 ± 3.2	64.30 ± 0.57
2 (upper-right)	139.23 ± 7.76	89.17 ± 2.8	66.75 ± 0.73
3 (lower-left)	138.58 ± 7.96	86.86 ± 3.5	65.35 ± 1.09
4 (lower-right)	137.99 ± 6.33	84.39 ± 2.9	64.27 ± 0.78
Mean	138.71 ± 7.14	86.94±3.11	65.17 ± 0.82
CV (%)	5.15	3.58	3.35

Supplementary Notes:

Supplementary Note 1. XPS curve-fitting protocols and constraints for O 1s and Zr 3d spectra.

1. Instrumentation and data acquisition. X-ray photoelectron spectroscopy (XPS) measurements were performed on a Thermo Scientific Escalab 250Xi spectrometer equipped with a hemispherical electron energy analyzer and a monochromatic Al Kα X-ray source (1486.6 eV). High-resolution regional spectra were acquired in the constant analyzer energy (CAE) mode with a pass energy of 20.0 eV and an energy step size of 0.100 eV.

2. Charge referencing and energy calibration. All binding energies were charge-referenced to the adventitious carbon C 1s peak (C–C) at 284.8 eV using the “Charge Shift” function in Thermo Scientific Avantage v6.9.0 with the “Shift by Amount” option. The same energy shift was uniformly applied to all regional spectra (O 1s, Zr 3d, C 1s, N 1s) from each sample.

3. Background subtraction and peak shape (Table S5). Prior to curve-fitting, a Shirley-type background was subtracted from all spectra using Avantage's built-in "Smart Background" algorithm. Peak deconvolution was performed using a Gaussian–Lorentzian product function (GL Product) with a fixed

Lorentzian/Gaussian (L/G) mix of 30% (i.e., 30% Lorentzian and 70% Gaussian contribution). The fitting algorithm was Simplex with a maximum of 1×10^5 iterations and a convergence criterion of < 0.01.

4. General fitting constraints. For all high-resolution spectra, the following constraints were applied to ensure physical meaningfulness:

- Full width at half maximum (FWHM): constrained to 1.2–1.8 eV for all sub-peaks;
- Binding energy tolerance: peak positions were allowed to vary within ±0.2 eV from their initial literature values;
- FWHM difference between adjacent sub-peaks: limited to ≤ 0.3 eV.

5. O 1s deconvolution details. The O 1s envelope was deconvoluted into four components based on the chemical environment of oxygen in the TPU/MOF-808/PEI composite system. The initial binding energies and assignments are summarized in Supplementary Table S6. All four components were fitted with identical L/G mix (30%) and independent FWHM values constrained within 1.2-1.8 eV. The total area of the deconvoluted spectrum was normalized to 100%, and the relative area percentage of each component was reported with standard deviation based on three independent measurements.

6. Zr 3d deconvolution details. The Zr 3d region was deconvoluted considering the spin-orbit splitting characteristic of Zr 3d orbitals. The following rigid constraints were applied during fitting (Table S7):

- Spin-orbit splitting: The energy separation between Zr $3d_{5/2}$ and Zr $3d_{3/2}$ was fixed at 2.43 eV (typical for Zr–O bonding in MOF-808 and ZrO_2-based materials);
- Area ratio: The integrated peak area of Zr $3d_{5/2}$ to Zr $3d_{3/2}$ was constrained to 3:2 (theoretical spin-orbit branching ratio);
- FWHM coupling: The FWHM of Zr $3d_{3/2}$ was constrained to be equal to that of Zr $3d_{5/2}$ to maintain physical consistency for the same chemical species.

7. Goodness of fit and reproducibility. The reliability of all deconvolutions was assessed by the R-factor (residual factor), which was consistently < 0.05 for both O 1s and Zr 3d spectra across all samples (SSD-NM, single-layer TPU control, and MOF-808 powder). All fitting constraints were applied consistently across the sample series to ensure comparability of relative peak areas.

Table S5. General XPS curve-fitting parameters for high-resolution O 1s and Zr 3d spectra.

Parameter	**O 1s**	**Zr 3d**
Background	Shirley-type (Smart Background)	Shirley-type (Smart Background)
Peak function	GL Product	GL Product

L/G mix	30% Lorentzian	30% Lorentzian
FWHM constraint	1.2–1.8 eV	1.2–1.8 eV
Binding energy tolerance	±0.2 eV	±0.2 eV
Special constraints	—	Spin-orbit splitting = 2.43 eV

Table S6. XPS O 1s deconvolution parameters for SSD-NM and single-layer 12/5 control.

O 1s Component	**SSD-NM**	**12/5**
Zr–O	530.2 ± 0.2 eV; FWHM: 1.3 eV	530.2 ± 0.2 eV; FWHM: 1.2 eV
C=O (non-H-bonded)	531.5 ± 0.2 eV; FWHM: 1.4 eV	531.6 ± 0.2 eV; FWHM: 1.4 eV
H-bonded O (C=O···H–N)	532.7 ± 0.2 eV; FWHM: 1.5 eV; Area: 23.02%	532.8 ± 0.2 eV; FWHM: 1.6 eV; Area: 2.63%
C–O / C–OH / H_2O	533.3 ± 0.2 eV; FWHM: 1.6 eV	533.4 ± 0.2 eV; FWHM: 1.7 eV
R-factor / Goodness of fit	< 0.05	< 0.05

Table S7. XPS Zr 3d deconvolution parameters for SSD-NM before and after DMMP exposure.

Zr 3d Component	**Pre-DMMP**	**Post-DMMP**
Zr 3d$_{5/2}$ (Zr^{4+}–O)	182.3 ± 0.2 eV; FWHM: 1.4 eV	182.6 ± 0.2 eV; FWHM: 1.4 eV
Zr 3d$_{3/2}$ (Zr^{4+}–O)	185.0 ± 0.2 eV; FWHM: 1.4 eV	184.7 ± 0.2 eV; FWHM: 1.4 eV
ΔE (3d$_{5/2}$ – 3d$_{3/2}$)	2.43 eV (fixed)	2.43 eV (fixed)
Chemical shift (ΔBE)	—	-0.3 eV
Assignment	Zr^{4+} in MOF-808 Zr$_6$-oxo cluster	Zr^{4+}···O=P (DMMP P=O coordinated, electron density increased)

Supplementary Note 2. Equivalent Capillary Model and Young-Laplace Calculation for Liquid Breakthrough Pressure.

1. Model assumptions. The pore network in electrospun nanofibrous membranes consists of irregular inter-fiber voids. To quantitatively correlate the maximum pore size with liquid breakthrough behavior, an equivalent capillary model is adopted, in which the irregular pores are simplified as a bundle of cylindrical capillaries with identical breakthrough characteristics. The maximum pore diameter (d_{max}), determined by the bubble-point method (or mercury intrusion porosimetry), is taken as the equivalent capillary diameter. The critical breakthrough pressure (P_b) is described by the Young-Laplace equation:

$$P_b = \frac{4\gamma_L|\cos\theta|}{d_{max}}\#(1)$$

where γ_L is the surface tension of water (72.8 mN·m^{-1} at 20°C), and θ is the static contact angle, and d_{max} is the maximum pore diameter obtained from Table S1.

Calculated results for each sample:

- 12/0: d_{max} = 1.74 μm, θ = 120.5°, $|\cos\theta|$ = 0.508. $P_{b,theo}$ ≈ 85 kPa. Measured hydrostatic pressure = 76.93 kPa. Ratio = 91%.
- 12/3: d_{max} = 1.41 μm, θ = 123.7°, $|\cos\theta|$ = 0.555. $P_{b,theo}$≈ 115 kPa. Measured = 75.17 kPa. Ratio = 66%.
- 12/5: d_{max} = 1.41 μm, θ = 125.6°, $|\cos\theta|$ = 0.582. $P_{b,theo}$ ≈ 120 kPa. Measured = 82.73 kPa. Ratio = 69%.
- 12/7: d_{max} = 3.47 μm, θ = 127.1°, $|\cos\theta|$ = 0.603. $P_{b,theo}$ ≈ 51 kPa. Measured = 7.99 kPa. Ratio = 16%.
- SSD-NM: d_{max} = 1.21 μm, θ = 126.1°, $|\cos\theta|$ = 0.589. $P_{b,theo}$ ≈ 142 kPa. Measured = 89.22 kPa. Ratio = 63%.

Physical interpretation of the measured-to-theoretical ratio. For the pristine TPU membrane (12/0), the ratio approaches unity (~92%), confirming high model fidelity for uniform polymer electrospun membranes with well-defined pore structures. For MOF-loaded single-layer fabrics (12/3, 12/5) and the SSD-NM sandwich architecture, the ratio falls to 63–69%, consistent with inherent deviations caused by non-cylindrical slit-like pore geometry, local fiber compressibility under hydraulic load, and pore interconnectivity that enables preferential flow along the path of least resistance. These effects are intrinsic to nanofibrous media and do not invalidate the model; rather, the consistency of the ratio across 12/5 and SSD-NM confirms that interlayer fusion does not introduce new percolating defects. The anomalously low ratio for 12/7 (~16%) indicates catastrophic failure via through-thickness percolating defect networks rather than ideal pore breakthrough, validating the use of d_{max} as a critical threshold parameter for liquid barrier design.

Supplementary Note 3. Diffusion Regime Analysis of Water Vapor in SSD-NM.

1. Knudsen number and diffusion regime. The transport mechanism of water vapor through membrane pores is determined by the Knudsen number (Kn), defined as the ratio of the molecular mean free path (λ) to the characteristic pore diameter (d_p):

$$Kn = \frac{\lambda}{d_p} \#(2)$$

At standard temperature and pressure (STP, 25 °C, 1 atm), the mean free path of water vapor molecules in air is approximately $\lambda \approx 100$ nm, as estimated from kinetic theory:

$$\lambda = \frac{k_B T}{\sqrt{2}\pi d_m^2 P} \#(3)$$

where k_B is the Boltzmann constant, T = 298.15 K, $d_m \approx 2.65 \times 10^{-10}$m is the collision diameter of H_2O, and $P = 1.013 \times 10^5$ Pa.

For SSD-NM, the average pore diameter is d_p = 0.80 – 0.94 μm and the maximum pore diameter is d_{max} = 1.21 μm. The corresponding Knudsen numbers are:

- For d_p = 0.80 μm: $Kn = 100 \times 10^{-9}/0.80 \times 10^{-6} \approx 0.125$
- For d_p = 0.94 μm: $Kn = 100 \times 10^{-9}/0.94 \times 10^{-6} \approx 0.106$
- For d_p = 1.21 μm: $Kn = 100 \times 10^{-9}/1.21 \times 10^{-6} \approx 0.083$

According to the IUPAC classification for gas transport in porous media:

- $Kn < 0.01$: continuum (Fick) diffusion regime;
- $0.01 < Kn < 1$: transition regime;
- $Kn > 1$: Knudsen diffusion regime.

Thus, SSD-NM operates in the **transition regime near the continuum limit**, where Fick diffusion remains the dominant mechanism and the diffusion coefficient exhibits weak dependence on pore diameter.

2. Effective diffusion coefficient. In the transition regime, the effective diffusion coefficient (D_{eff}) is described by the Bosanquet equation:

$$\frac{1}{D_{eff}} = \frac{1}{D_{Fick}} + \frac{1}{D_{Kn}} \#(4)$$

where $D_{Fick} \approx 2.5 \times 10^{-5}$ m^2 s^{-1} is the bulk diffusion coefficient of water vapor in air at STP, and D_{Kn} is the Knudsen diffusion coefficient. For cylindrical pores, D_{Kn} is expressed as:

$$D_{Kn} = \frac{d_p}{3}\sqrt{\frac{8RT}{\pi M}} \#(5)$$

where R = 8.314 J mol^{-1}, M=0.018 kg mol^{-1} is the molar mass of water, and the mean molecular velocity

$\bar{v} = \sqrt{8RT/\pi M} \approx 592$ m s^{-1} at 25 °C.

For d_p = 0.80 µm:

$$D_{Kn} = \frac{0.80 \times 10^{-6}}{3} \times 592 \approx 1.58 \times 10^{-4} \text{ m}^2 \text{ s}^{-1}$$

Since $D_{Kn} \approx 6.3D_{Fick}$, substitution into Eq. (4) yields:

$$\frac{1}{D_{eff}} = \frac{1}{D_{Fick}} + \frac{1}{6.3D_{Fick}} = \frac{1.16}{D_{Fick}} \#(6)$$

$$D_{eff} \approx 0.86D_{Fick} \#(7)$$

Therefore, reducing the pore diameter from 0.94 µm to 0.80 µm decreases the Knudsen diffusion coefficient by approximately 15%; however, because , the effective diffusion coefficient decreases by less than 3% (from ~0.88 to ~0.86). This extremely weak pore-size dependence confirms that the observed ~15% WVTR reduction in SSD-NM cannot be attributed to intrinsic diffusion resistance from pore narrowing; instead, it is primarily governed by increased pathway tortuosity and PEI-induced water retention.

Supplementary Note 4. Humidity-dependent DMMP adsorption performance.

Experimental methods. DMMP vapor adsorption experiments under controlled relative humidity were conducted in a constant temperature and humidity laboratory. Membrane samples (2 cm × 2 cm) were pre-equilibrated at the target relative humidity (30%, 60%, or 90% RH) for 2 h to ensure moisture adsorption equilibrium, followed by exposure to DMMP saturated vapor (generated by natural evaporation of DMMP liquid at 25°C) for 1 h. Preliminary experiments confirmed that this duration was sufficient to achieve adsorption equilibrium. The adsorption capacity was determined gravimetrically by measuring the mass change before and after exposure. All experiments were performed at room temperature (~25°C), with each condition repeated independently (n = 3).

Results and discussion. As shown in Fig. S14, all samples exhibited a monotonically decreasing adsorption capacity with increasing relative humidity, consistent with the well-established competitive adsorption mechanism between water and DMMP molecules on porous surfaces. Water molecules physisorb onto fiber surfaces and within MOF pores under high-humidity conditions, forming a surface hydration layer that partially blocks the effective adsorption sites accessible to DMMP. At 90% RH, the adsorption capacities of TPU (12/0), 12/5, and SSD-NM decreased to approximately 49.30, 242.28, and 252.75 mg·g^{-1}, respectively. Nevertheless, SSD-NM maintained the highest absolute DMMP uptake across all humidity conditions, confirming that the sandwich architecture sustains a high DMMP enrichment capability even under humid environments.

Supplementary Note 5. Experimental Validation of the Alkaline Microenvironment in the PEI Intermediate Layer and Potentiometric Titration Characterization of Protonation-Deprotonation

Behavior.

To verify the role of PEI in constructing an alkaline microenvironment within the intermediate layer of the SSD-NM sandwich membrane and to elucidate its protonation-deprotonation equilibrium, validation experiments were conducted from three complementary perspectives: (1) direct measurement of the steady-state pH of the membrane-contacting solution using a micro-pH electrode; (2) qualitative visualization of the surface microenvironment via phenolphthalein indicator staining; and (3) quantitative analysis of amino-group proton binding and release by potentiometric titration.

1. Micro-pH Electrode Measurement. The SSD-NM sandwich membrane and the control membrane 12/5 (devoid of the PEI intermediate layer) were cut into pieces and accurately weighed to obtain identical masses (0.5 g each), followed by immersion in 25 mL of Deionized water. The samples were equilibrated under constant-temperature (25 °C) shaking for 24 h. A micro-pH electrode was employed to determine the steady-state pH of the equilibrated immersion solutions. Each sample was measured in triplicate, and the average value was recorded after the reading stabilized.

2. Phenolphthalein Indicator Staining. A 0.5 wt% phenolphthalein indicator solution was prepared in ethanol and uniformly dropped onto the surface of the above-equilibrated, wetted membranes. After standing for 30 s, the coloration was observed and photographed under white light. Phenolphthalein exhibits a characteristic fuchsia color in the pH range of 8.3-10.0 and remains colorless under neutral or acidic conditions, enabling direct qualitative discrimination of acidic versus alkaline microenvironments at the membrane interface.

3. Potentiometric Titration. Sample Preparation. Branched polyethyleneimine (PEI, $M_w \approx 1800$, 5 mg), the SSD-NM sandwich-membrane intermediate layer (~25 mg), a pure TPU membrane (12/0), and a 12/5 membrane were selected as test samples. Each sample was placed in 25 mL of ultrapure water, followed by the addition of 1 mL of 0.1 mol/L HCl solution to ensure complete protonation of the amino groups. The resulting titration solution had an initial total volume of 26 mL, with the initial pH stabilized in the range of 2.5-2.7.

Titration Procedure. Potentiometric titration was performed using an automatic titrator at a constant temperature of 25 °C, with a standardized 0.1 mol/L NaOH solution as the titrant. The titrant was added in 20 μL increments. After each addition, the solution was continuously stirred and allowed to stand until the pH reading stabilized completely; the cumulative volume of NaOH added and the corresponding pH were recorded synchronously. The titration was terminated when the system pH reached approximately 11 and remained stable.

4. Data Processing and Theoretical Calculations

(1) Protonation Degree (α) Calculation. Based on the Bjerrum difference charge-balance principle, the average proton binding number, $\bar{n}_\mathrm{H}$ is defined as:

$$\bar{n}_H = \frac{n_{total,NH} - n_{net,NaOH}}{n_{total,NH}} \#(8)$$

where $n_{total,NH}$ is the total amount of titratable amino groups in the system, determined from the difference between the titration end-point interval and the blank free strong-acid background; $n_{net,NaOH}$ is the net amount of NaOH consumed by the system at the corresponding pH after blank background subtraction.

The protonation degree is defined as $\alpha = \bar{n}_H$: $\alpha = 1$ corresponds to fully protonated amino groups, and $\alpha = 0$ corresponds to fully deprotonated amino groups, thereby characterizing the extent of proton binding and release of PEI amino groups at different pH values.

(2) Buffering Capacity (β) Calculation. The buffering capacity, β, is used to characterize the ability of a system to resist pH fluctuations. It is physically defined as the amount of strong base required to change the pH of a unit volume of solution by one unit, calculated using a discrete difference form:

$$\beta = \frac{C_{NaOH} \cdot \Delta V}{(V_0 + V) \cdot \Delta pH} \#(9)$$

where $C_{NaOH} = 0.1 \text{ mol·L}^{-1}$, ΔV is the incremental volume of the NaOH titrant; $V_0 = 26$ mL is the initial volume of the titration system, and $\bar{V}$ is the average cumulative volume of base added within the corresponding titration interval. The unit of buffering capacity is $\text{mmol·L}^{-1}\text{·pH}^{-1}$.

Because the titration is initiated in the presence of excess free HCl, the buffering contribution in the pH < 4.5 region primarily arises from the neutralization of free strong acid and does not reflect the intrinsic proton-dissociation behavior of PEI amino groups. Therefore, only data in the pH ≥ 4.5 interval were used to calculate and analyze the inherent buffering capacity characteristics of PEI and the composite systems. The buffering capacities for key pH intervals, calculated from the raw titration data, are summarized in Table S8

Table S8. Summary of Average Buffering Capacity (β) in Key pH Intervals.

pH Interval	**PEI *β* (mmol·L^{-1}·pH^{-1})**	**SSD-NM middle layer *β*(mmol·L^{-1}·pH^{-1})**	**12/5 *β* (mmol·L^{-1}·pH^{-1})**
4.5-5.5	0.71	0.45	< 0.05
5.5-6.5	0.44	0.33	< 0.05
6.5-7.5	0.45	0.36	< 0.05

pH Interval	**PEI β (mmol·L^{-1}·pH^{-1})**	**SSD-NM middle layer β(mmol·L^{-1}·pH^{-1})**	**12/5 β (mmol·L^{-1}·pH^{-1})**
7.5-8.5	0.71	0.43	< 0.05
8.5-9.5	0.68	0.57	< 0.05

References

1 J. Dai, D. Wang, J. Yang, R. Tian, Q. Wang and Y. Li, *J. Colloid Interface Sci.*, 2023, **652**, 1156–1169.

2 J. Y. Seo, M. H. Choi, B. W. Lee, J.-H. Lee, S. Shin, S. Cho, K. Y. Cho and K.-Y. Baek, *ACS Appl. Mater. Interfaces*, 2022, **14**, 50246–50255.

3 X. Wang, Y.-X. Zheng, C. Ding, M. Zhang, Z.-Z. Yu, S. Wang and D. Yang, *Adv. Funct. Mater.*, 2025, **35**, 2504379.

4 Z. Chen, K. Ma, J. J. Mahle, H. Wang, Z. H. Syed, A. Atilgan, Y. Chen, J. H. Xin, T. Islamoglu, G. W. Peterson and O. K. Farha, *J. Am. Chem. Soc.*, 2019, **141**, 20016–20021.

5 H. Liao, M. Liu, W. Ding, S. Yao, C. Zhu, H. Zhang, J. Sheng and Y. Yao, *ACS Appl. Nano Mater.*, 2025, **8**, 19609–19618.

6 G. Ren, Z. Li, L. Tian, D. Lu, Y. Jin, Y. Zhang, B. Li, H. Yu, J. He and D. Sun, *Colloids and Surfaces A: Physicochemical and Engineering Aspects*, 2023, **658**, 130643.

7 D. Lu, Y. Li, Y. Chai, X. Wen, L. Chen and S. Sun, Fibers, 2025, **13**, 105.

8 B. Zhang, X. Li, Y. Lin, N. Cheng, W. Jiao, X. Wang, J. Yu and B. Ding, *Polymers*, 2025, **17**, 486.

9 L. Zhang, J. Sheng, Y. Yao, Z. Yan, Y. Zhai, Z. Tang and H. Li, *Polymers*, 2022, **14**, 5295.